Approaches to Mid-Infrared, Super-Resolution Imaging and Spectroscopy

Ilia M. Pavlovetc,[1] Kyle Aleshire,[1] Gregory V. Hartland,[1,*] Masaru Kuno[1,2,*]

[1] Department of Chemistry and Biochemistry, University of Notre Dame, Notre Dame, IN 46556 USA
[2] Department of Physics, University of Notre Dame, Notre Dame, IN, 46556 USA

Abstract: This perspective highlights recent advances in super-resolution, mid-infrared imaging and spectroscopy. It provides an overview of the different near field microscopy techniques developed to address the problem of chemically imaging specimens in the mid-infrared "fingerprint" region of the spectrum with high spatial resolution. We focus on a recently developed far-field optical technique, called infrared photothermal heterodyne imaging (IR-PHI), and discusses the technique in detail. Its practical implementation in terms of equipment used, optical geometries employed, and underlying contrast mechanism are described. Milestones where IR-PHI has led to notable advances in bioscience and materials science are summarized. The perspective concludes with a future outlook for robust and readily accessible high spatial resolution, mid-infrared imaging and spectroscopy techniques.

Introduction:

Infrared (IR) imaging and spectroscopy is an important technique for identifying chemical specimens and elucidating their structure. This stems from characteristic "fingerprint" vibrational signatures unique to molecules, which exquisitely report on chemical bonding. In terms of sensitivity, IR imaging and spectroscopy exhibits clear advantages over Raman-based microscopies due to vibrational absorption cross sections (σ) 10-12 orders of magnitude larger than corresponding Raman scattering cross sections. Because of lower σ-values, analytical Raman microscopy measurements often employ special substrates that exploit plasmonic enhancements of local fields to boost Raman signals.[1]

Despite its advantages, IR imaging/spectroscopy is hindered by its poor spatial resolution and consequently has not found as wide use as Raman microscopy. Traditional IR measurements are limited by the optical diffraction limit. For mid-infrared (mid-IR) radiation, a practical spatial resolution between 3-10 μm is expected. Application of mid-IR absorption imaging and spectroscopy to problems involving modern, condensed phase systems is therefore limited to measurements conducted on micron length scale specimens. This hinders applications of IR imaging and spectroscopy in nanoscience as well as in biology, where chemical heterogeneities as well as crowded spectroscopic environments demand high spatial resolution analytical techniques.

Achieving mid-infrared chemical imaging below the infrared diffraction limit:

Scanning infrared near field optical microscopy (IR-SNOM). To circumvent these limitations, a number of near- and far-field infrared approaches have recently been developed. A first approach is IR scanning near field optical microscopy (IR-SNOM).[2,3,4,5] IR-SNOM has two operating modalities: (i) Apertured IR-SNOM where mid-IR radiation is focused onto specimens through a metal-coated optical fiber with sub-wavelength aperture of order $\lambda/100$. Subsequently scattered mid-IR light is then collected with the same fiber, or alternatively with a reflective objective in the far field.[3,4] (ii) Apertureless IR-SNOM where a sharp metallized tip creates highly localized electric fields at the sample[6] and sample-scattered light is collected in far field. Near field absorption is deduced indirectly through changes to the amount of sample-scattered mid-IR light.[7,8]

Apertured IR-SNOM. In apertured IR-SNOM the signals scale as $(a/\lambda)^4$ where a is the aperture radius and λ is the incident IR wavelength.[3] This fourth power dependency restricts experimental values of a and, in turn, means that practical limits exist to apertured IR-SNOM's spatial resolution. Beyond this and perhaps of greater significance, the intrinsically low optical throughput of near field tips (10^{-3}) requires that high brightness, mid-infrared light sources be used.[3] Despite these restrictions, apertured IR-SNOM has been successfully implemented to image chemical heterogeneities in polystyrene/polyethyl acrylate thin films with a 300 nm ($\lambda/20$) spatial resolution.[9] Researchers have also imaged cubic, wurtzite and hexagonal phase inhomogeneities in boron nitride thin films through local differences in transverse optical phonon energies.[10] On the biological side, apertured IR-SNOM's high spatial resolution has been used to investigate DNA localization within nuclei of individual keratinocyte cells with a $\lambda/60$ resolution[5] as well as distinguish cancerous from normal oesophageal cells.[4]

Apertureless IR-SNOM. Work on apertureless IR-SNOM dates back to 1996[6] with Lahrech using a CO_2 laser as the excitation source to establish contrast differences on a Au/Si grating. Subsequent studies have employed CO_2/CO,[6,11,12,13,14] free electron[15,16] and quantum cascade lasers (QSLs)[17] as excitation sources. Mid-IR supercontinuum laser sources have more recently been used to measure apertureless IR-SNOM spectra in FTIR-like fashion.[18,19] Two notable exceptions to the use of high brightness mid-IR sources are the apertureless IR-SNOM experiments by O'Callahan *et al*. and Wagner *et al.*. In the former case, O'Callahan *et al*. have successfully used a blackbody source to spectrally resolve the transverse optical phonons of hexagonal boron nitride platelets.[20] In the latter case, Wagner *et al.* have implemented an incoherent plasma, thermal IR emitter to spectrally resolve the phonon and surface phonon-polariton peaks of 20 nm thick boron nitride nanotubes.[21] Other successful implementations of apertureless IR-SNOM include mapping the secondary structure of single proteins to illustrate protein orientation-dependent spectral differences,[22] and visualizing plasmonic "hot-spots" of individual IR gap antennas.[23] An important point to note is that extracting spectral information from apertureless IR-SNOM data is not trivial, as both scattering and absorption contribute to the measured signal.[7,8,24,25,26]

Synchrotron infrared nanospectroscopy (SINS). A variation of apertureless IR-SNOM is synchrotron infrared nanospectroscopy (SINS).[27] Distinguishing SINS from apertureless IR-SNOM is the use of a high brightness *broadband* source that enables rapid Fourier transform infrared (FTIR)-based spectral extraction.[27,28] Milliron has recently applied SINS to measure the mid-IR plasmon resonances of individual, doped semiconductor nanocrystals.[28] These measurements have revealed ultranarrow, localized surface plasmon resonances with linewidths of order 70 meV. The study highlights the long plasmon dephasing times possible in the mid-IR, stemming from suppressed radiation damping.[28] **Figure 1a** summarizes experimental realizations of IR-SNOM and SINS.

Scanning transmission electron microscopy electron energy loss spectroscopy (STEM-EELS). A second general technique explored to achieve high spatial resolution, mid-infrared imaging/spectroscopy is scanning transmission electron microscopy electron energy loss

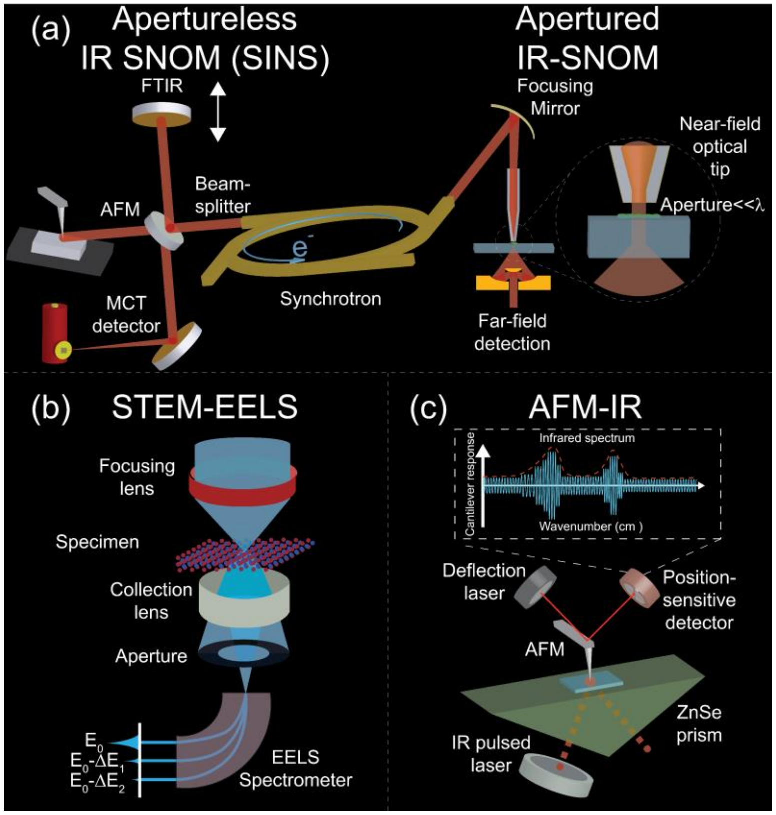

Figure 1. Illustrations of various super-resolution, mid-infrared imaging and spectroscopy techniques. (a) apertureless IR-SNOM (SINS) and apertured IR-SNOM, (b) STEM-EELS, and (c) AFM-IR.

spectroscopy (STEM-EELS).[29,30] STEM-EELS assesses sample absorption through the energy loss of incident electrons in a transmission electron microscope (TEM). STEM-EELS has been used to image electronic transitions in dielectric thin films,[31] the bulk and surface plasmon resonances of individual silver nanoparticles[32], and energy transfer between plasmonic nanoparticles and semiconductor substrates.[33] Characteristic energy losses in these measurements range from 2.0-7.5 eV. The high spatial resolution (up to 1 Å[34]) intrinsic to STEM-EELS has also allowed researchers to spatially and energetically resolve localized surface plasmon resonance hot spots in surface enhanced Raman scattering-active nanostructures.[35]

Only recently has mid-IR imaging and spectroscopy become possible with STEM-EELS. This is due to advances in electron monochromator technologies that make possible highly monochromatic electrons with energy dispersions below 50 meV.[34] Consequently, mid-IR spectroscopy measurements up to 370 cm^{-1} away from the zero loss beam are now possible.[36] **Figure 1b** visually summarizes the implementation of STEM-EELS in a TEM. Notable accomplishments of mid-IR STEM-EELS include imaging the plasmon resonances of straight/branched silver nanowires,[29] and quantitative measurements of quality factors as well as dephasing times of various plasmonic gold nanostructures.[37] Mid-IR STEM-EELS has also been used to distinguish bulk from surface phonon modes in individual MgO nanocubes.[38] However, STEM-EELS cannot be applied to electron beam sensitive samples, or those in aqueous/ambient environments. Additionally, only thin specimens can be imaged. These restrictions preclude the use of STEM-EELS in biological imaging. Furthermore, the need for highly monochromatic electrons necessitates specialized instrumentation not commonly found in academic laboratories.

AFM-IR. A third technique to realize high spatial resolution mid-IR imaging/spectroscopy is atomic force microscopy infrared (AFM-IR) imaging. In AFM-IR, an AFM tip probes the thermal expansion induced in a specimen by absorption of infrared radiation.[39,40,41] The sensitivity of AFM-IR derives from the inherit sub-nm height resolution of AFM, which yields sensitivity to small thermal expansions and, by extension, infrared absorption. This has enabled acquisition of IR spectra from small ensembles (~300) of molecules.[42]

AFM-IR's spatial resolution is, in principle, dictated by the AFM tip radius. Consequently, a resolution as small as 1 nm[43] is possible. However, the technique's signal contrast comes from topographical changes due to thermal expansion. Spatial resolution is therefore dictated by a convolution of the AFM's resolution with the thermal diffusion length of a particular experiment. Consequently, a spatial resolution of order 20 nm is commonly achieved in practice.[39]

AFM-IR's high spatial resolution has found use in plasmonics where spatial differences in the absorption of IR light has been seen in individual, heavily-doped InAs micropillars.[44] It has also been used to measure the intersubband spectrum of single ~20 nm InAs quantum dots.[45] In layered two-dimensional nanostructures, Centrone and co-workers have used the technique to spatially-resolve organic contaminants on surfaces.[46] Finally, AFM-IR has found use in the life sciences to chemically characterize the internal structure of individual breast cancer cells.[47]

AFM-IR's primary drawback is that it requires the thermal expansion of specimens in order to detect infrared absorption. This means that experiments conducted on ~~condensed phase~~ samples having small thermal expansion coefficients becomes challenging. Lesser drawbacks include the need for AFM feedback electronics and the intrinsically limited field of view of AFM. **Figure 1c** outlines the AFM-IR technique.

Infrared photothermal heterodyne imaging

In contrast to the abovementioned techniques, there exists an all-optical, tabletop approach for measuring high spatial resolution, mid-infrared images and spectra of specimens under ambient conditions. Called infrared photothermal heterodyne imaging (IR-PHI), the technique uses a high brightness, tunable mid-infrared laser to excite samples. Subsequent non-radiative relaxation processes induce local temperature changes in and nearby absorbing species, which alter the refractive indices and scattering cross sections. The local temperature differences (ΔT) are of the order ΔT=1-50 K. Modulating the IR pump beam introduces periodic changes in the specimen's local refractive index with the typical magnitude of Δn being ~10^{-3}-10^{-4} for condensed phase (soft) materials/liquid specimens[48] and Δn~10^{-5}-10^{-6} [49] for metals and semiconductors. Periodic Δn changes ultimately induce intensity modulation in a second, continuous wave (CW) probe laser incident on the sample that can be detected with a lock-in amplifier. The probe modulation depth is proportional to the amount of pump light absorbed. More importantly, because a *visible* wavelength probe is used to detect pump-induced Δn changes, IR-PHI possesses a spatial resolution dictated by the visible diffraction limit.[50,51,52,53] Of note is that IR-PHI borrows heavily from corresponding, visible photothermal microscopies,[48,54,55,56] which have achieved single molecule sensitivity. The primary differences are the use of a high brightness, tunable mid-infrared pump laser, and the general absence of a photothermal medium~~,~~ surrounding the sample.

IR-PHI Pump. In practice, IR-PHI uses a tunable, mid-infrared laser to induce local heating in the sample. Both QCL[52,57,58,59] and optical parametric oscillator (OPO)-based systems[53,60,61] have been used. Advantages of QCLs include their rapid frequency tunability (~10,000 cm^{-1}/s), DC-to-MHz variable repetition rates and narrow linewidths of order 0.1 cm^{-1}. Disadvantages include limited, single box tuning ranges (~150 cm^{-1}), although multiple QCLs can be combined to realize broader spectral ranges. For OPO systems, advantages include extremely broad (single box) frequency tuning ranges (up to 1,600 cm^{-1}) and generally higher average powers (up to 1 W). Disadvantages include fixed repetition rates, slower tuning speeds (100 cm^{-1}/s), and relatively large output linewidths of order ~10 cm^{-1}. An additional way to extend the spectral range of IR-PHI involves difference frequency generation (DFG), as demonstrated by several groups.[51,62]

IR-PHI Probe. For both visible PHI and IR-PHI, a visible, CW probe detects pump-induced changes to n, i.e. Δn. As with visible PHI a number of CW sources have been employed. Example IR-PHI probes include diode and Nd:YAG (λ_{probe}=532-1064 nm),[53,60] Ti:Sapphire (λ_{probe}=800 nm),[52,57,59] and HeNe gas (λ_{probe}=632.8 nm) lasers.[63] The primary restriction for the probe is that its frequency not overlap with an optical transition of the ~~analyte~~ sample. This, however, is not a hard restriction and visible PHI has been successfully demonstrated in cases where the probe is resonant with the sample absorption.[64]

IR-PHI experimental pump and probe geometries. **Figure 2** summarizes the two general pump/probe geometries employed in IR-PHI. In **Figure 2a**, a counter-propagating geometry is outlined where pump and probe beams are incident on the sample from opposing sides. **Figure 2b** shows the more traditional, co-propagating pump/probe geometry where a single objective (usually a reflective Cassegrain objective) focuses collinear pump and probe beams onto the sample, and reflected probe light is collected with the same objective. In what follows, we discuss the advantages, disadvantages, and critical differences of these two geometries.

In the counter-propagating geometry (**Figure 2a**), opposing pump and probe beams require that substrates on which the specimens sit to be transparent for at least one of the beams. Consequently, CaF$_2$[58,60] and ZnSe[50,53,65] have been used as substrate materials. This stems from their wide visible and infrared wavelength transparencies [CaF$_2$: 200 nm-8.0 μm; ZnSe: 600 nm-13.0 μm]. The primary motivation for conducting IR-PHI using a counter-propagating pump/probe geometry is the freedom to employ high numerical aperture (NA) refractive objectives to focus the probe beam onto the sample. Highlighting this are NA-values as large as NA=1.49 for oil immersion objectives. Even dry refractive objectives can have NA-values between 0.90 and 0.95. By

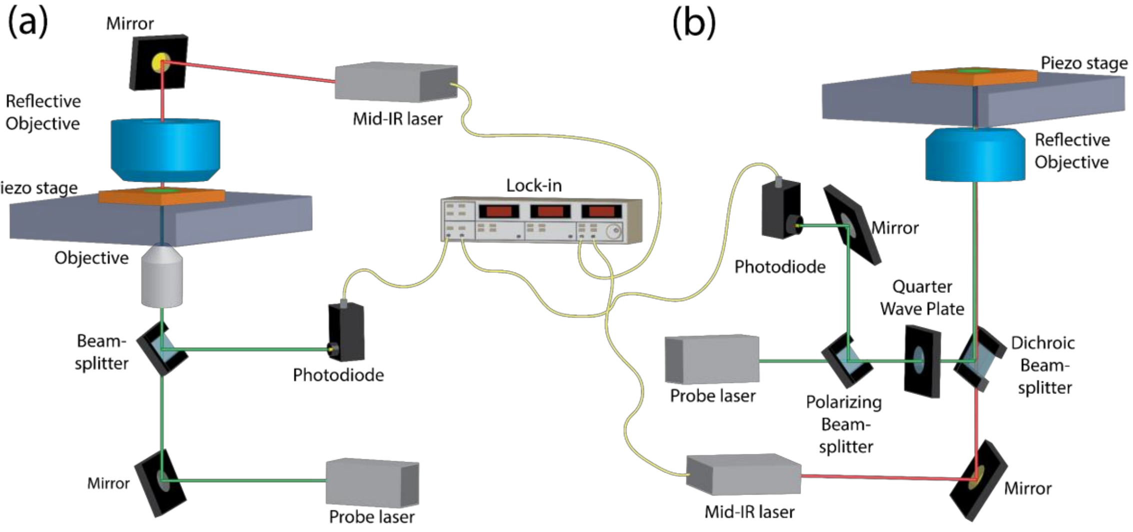

Figure 2. Basic layout of IR-PHI in its (a) counter- and (b) co-propagating pump/probe geometries.

contrast, commercial reflective objectives have a maximum NA-value of NA=0.80. Consequently, a sizable improvement in resolution becomes possible when the probe beam is focused using refractive as opposed to a reflective objective. Highlighting this is a study by Li *et al.*[53] who have demonstrated a spatial resolution of ~300 nm when using a 532 nm probe. The achieved resolution is a 20-fold improvement over the IR diffraction limit, ~7 μm.

The use of counter-propagating geometry also opens the door to various hybrid techniques, of which one example involves combining IR-PHI with Raman spectroscopy.[66] Proof-of-concept has been demonstrated by acquiring comprehensive IR absorption and Raman information of single bacteria with submicrometer resolution.

In the co-propagating IR-PHI geometry (**Figure 2b**), a common reflective objective focuses both the pump and probe beams onto the sample. Because of the lower maximum NA of reflective objectives, the spatial resolution of co-propagating IR-PHI is lower. For example, Zhang *et al.*[52] have demonstrated a spatial resolution of 600 nm when using a 785 nm probe wavelength. This highlights the fact that reflective objectives[67] can yield higher spatial resolution than expected from the Abbe criterion.[68]

An additional inconvenience of co-propagating IR-PHI is the need to control the incident probe polarization to properly detect the modulated photothermal signal.[50] Typically a linearly polarized probe beam is first sent through a polarizer and quarter waveplate prior to the microscope objective (**Figure 2b**). The quarter waveplate makes the incident probe beam circularly polarized with a given handedness. Following interaction with the sample and reflection off the substrate, a phase shift occurs. The scattered light's circular polarization consequently converts to the opposite handedness. Upon passage through the quarter waveplate, the probe polarization reverts back to linear, albeit with a polarization orthogonal to that of the original, incident probe beam.[68] Subsequent passage through the polarizer diverts the modulated probe light onto a photodiode.[5048]

IR-PHI signal detection. Practical detection of IR-PHI signals involve spectrally filtering the collected probe light followed by lock-in detection at the IR pump modulation frequency. Because pump intensities can be modulated at high frequencies (up to 1 MHz is possible), the IR-PHI signal is detected at a frequency where 1/f noise is negligible. This enables sensitive, lock-in detection of infrared absorption with high signal-to-noise ratios.

IR-PHI images are traditionally obtained by raster scanning the sample through the pump and probe foci using a piezo stage. At each point during the scan, a lock-in amplifier reads the collected probe signal where, in most cases, the signal comes directly from an avalanche photodiode.[53,63] Autobalanced photodetectors[60,69] can also be used to suppress probe laser intensity fluctuations if needed. Lock-in readings are generally made at the fundamental modulation frequency (i.e. at 1f). For images, the signal is acquired on a point-by-point basis to construct a two-dimensional image. For local infrared absorption spectra, the piezo stage is positioned at a desired spatial coordinate and the IR-PHI signal is recorded as a function of pump wavelength. Control studies have shown that IR-PHI spectra reproduce FTIR spectra of samples with high fidelity.[52,53,57,58]

IR-PHI contrast mechanism. Although a detailed mechanism for IR-PHI signal generation is still being investigated, heterodyning of the reflected probe light with the corresponding intensity-modulated signal component is generally thought to be the reporter of IR-PHI contrast. The associated probe modulation depth carries information about the relative amount of infrared absorption and, though not quantitative, directly reports on the absorption coefficient of the sample. Beyond this, there exists some uncertainty as to the microscopic origin of IR-PHI contrast.

In this regard, at least two contributions have been suggested: Δ*T*-induced Δ*n* in samples[56,70] and Δ*T*-induced changes to a specimen's scattering cross section through small changes to its physical size.[53] At present the relative contributions of these effects are unknown. It is worth noting that because IR-PHI is photothermal in nature, only *absorbed* pump light contributes to the measured signal. This is in contrast to other single particle microscopy techniques, such as spatial modulation microscopy/spectroscopy[69,71,72,73,74,75] and polarization modulation microscopy,[76,77] which measure sample *extinction* (i.e. absorption and scattering).

IR-PHI milestones

We now illustrate several developmental milestones where IR-PHI's super-resolution infrared imaging capabilities have been demonstrated, and where it has led to notable achievements in bioscience and materials science.

First experimental demonstration of IR-PHI. Lee at al. were the first to demonstrate all-optical, photothermal-based, mid-infrared imaging. In their 2009 paper,[50] individual droplets of balsamic oil in water were imaged using the oil's aliphatic (symmetric) CH_2 stretch at 2850 cm^{-1}. Mid-IR pump light in the study was generated through difference frequency generation (DFG). Specifically, the 1064 nm fundamental of a Nd:YVO_4 laser was upconverted to 786-817 nm using an OPO. The 1064 nm fundamental and 786-817 nm light from the OPO were then passed through a DFG crystal to obtain mid-IR light with wavelengths between 2.87-3.57 μm. Residual 786-817 nm light was then used as the probe in subsequent mid-IR photothermal measurements. **Figure 3a** (**3b**) shows a representative IR-PHI image of an individual oil droplet (water) acquired by Lee *et al*. using its 2850 cm^{-1} (3333 cm^{-1}) symmetric CH_2 stretch (OH stretch). **Figure 3c** shows corresponding FTIR spectra of balsamic oil and water with the monitored transitions indicated with arrows.

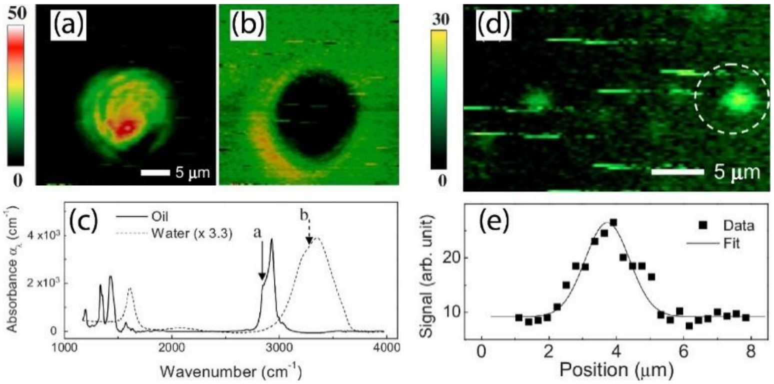

Figure 3. IR-PHI image of (a) a balsamic oil droplet in water acquired using its 2850 cm^{-1} symmetric CH_2 stretch and (b) the same area imaged using water's 3333 cm^{-1} OH stretching mode. (c) Corresponding FTIR spectra. (d) Super-resolution IR-PHI image of a water droplet in balsamic oil imaged at 3333 cm^{-1} (circled). (e) Associated linescan showing an achieved spatial resolution of 1.1 μm. Reprinted from https://doi.org/10.1063/1.3167286, with the permission of AIP Publishing.

Figure 3d illustrates the sub IR diffraction limit spatial resolution achieved in the acquired images. Specifically, an individual water droplet with a ~1 μm diameter is circled. **Figure 3e** shows its corresponding linescan and reveals an experimental spatial resolution of 1.1 μm. Given that the employed mid-IR wavelength was 3.5 μm and the objective had a NA=0.5, the data indicates a three-fold improvement in spatial resolution over the mid-IR diffraction limit. Of note is that this study has gone relatively unnoticed for nearly a decade. This is possibly due to suggestions in the title that the observed contrast arises from nonlinear refraction, despite the use of low excitation intensities, as opposed to a more conventional photothermal effect.

Counter-propagating IR-PHI. The next major advance in the development of IR-PHI came in 2017 when Li *et al*. demonstrated the use of a counterpropagating pump and probe beam geometry to dramatically enhance the spatial resolution of the technique. As described earlier in more detail, this geometry allows visible probe light to be focused onto the sample independently of the pump, using high NA *refractive* objectives. This is key as NA-values as large as 1.49 are possible through use of oil immersion objectives. **Figure 4a** shows a resulting IR-PHI image of a single *d*=100 nm polystyrene bead, acquired using it 3030 cm^{-1} (asymmetric) CH_2 stretch. The associated linescan in **Figure 4b**, shows an achieved resolution of ~300 nm using a 532 nm probe and a NA=0.9 objective. In the same study, IR-PHI's capability to acquire super-resolution images and spectra over wide areas was demonstrated. **Figure 4c** illustrates an acquired 100×100 μm^2 IR-PHI image of patterned polymethylmethacrylate (PMMA) imaged using its 3000 cm^{-1} CH_2 asymmetric stretch.

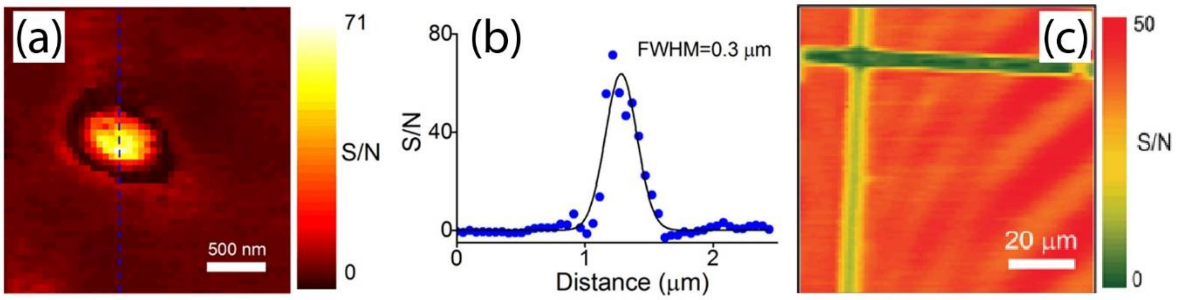

Figure 4. (a) IR-PHI image of an individual *d*=100 nm polystyrene bead imaged using its asymmetric CH_2 3030 cm^{-1} stretching mode. (b) Corresponding linescan of the same bead in (a). (c) Large area IR-PHI image of patterned PMMA imaged using its 3000 cm^{-1} asymmetric CH_2 stretching mode. Adapted with permission from https://pubs.acs.org/doi/full/10.1021/acs.jpcb.7b06065. Copyright 2019 American Chemical Society.

Dynamics using stop motion IR-PHI. In 2018, Cho and co-workers successfully applied co-propagating IR-PHI to image cell dynamics in a stop motion fashion.[63] The experiment used a tunable QCL for the pump and a 632.8 nm HeNe laser as the probe. Both lasers were made collinear using a dichroic beamsplitter and were then focused onto the sample using a reflective, NA=0.66 objective. The achieved spatial resolution was 540 nm. Samples were raster scanned over 50×50 μm^2 areas with a 5 minute acquisition time per image.

Figure 5 shows time-lapse images of an individual oligodendrocyte cell undergoing cell division. Images were acquired over the course of two hours without any cell photodamage or apparent changes to its replication behavior. Additionally, observed contrast differences in the images stem from changes to protein localization during replication. The work thus highlights the ability of IR-PHI to reveal intracellular structure dynamics in a label free manner.

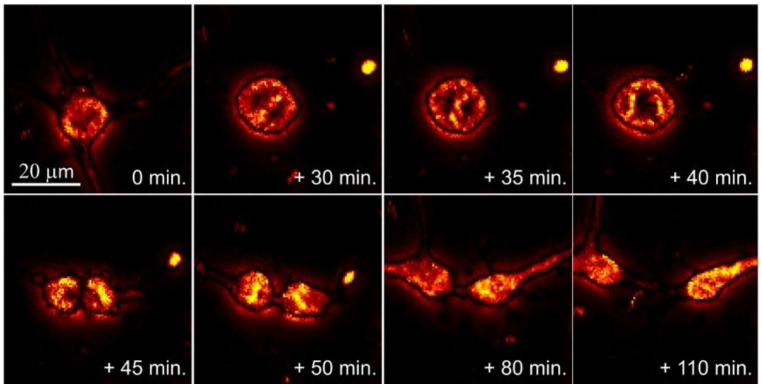

Figure 5. IR-PHI time-lapse imaging of an individual oligodendrocyte cell undergoing cell division. Images acquired at different times, highlighting the cell's normal (0 min), metaphase (+30 min), and cytokinesis (+50 min) states. Images acquired using the 1650 cm^{-1} protein amide band. Adapted with permission from https://pubs.acs.org/doi/abs/10.1021/acs.jpclett.9b00616. Copyright 2019 American Chemical Society.

Widefield IR-PHI. During the same year, a widefield imaging modality was introduced to IR-PHI by Cheng and co-workers.[61] Although prior IR-PHI studies established its high spatial resolution as well as capacity for observing dynamics, images were generated via specimen raster scanning. Consequently, fundamental limitations to monitoring dynamic processes exist given the finite time required to scan an area. For Cho and co-workers, this was 5 minutes for a 50×50 µm^2 region.[63] More crucially, temporal differences exist between pixels in raster scanned images. Widefield IR-PHI therefore represents a notable development as photothermal signals from *all* areas of a given specimen are acquired simultaneously. More relevantly, image acquisition can be much faster, making possible the real time, mid-IR imaging of specimens with chemical specificity.

The fundamental departure from traditional IR-PHI is the use of a complementary metal–oxide–semiconductor (CMOS) camera to detect pump-induced, photothermal changes in a specimen. In practice, the pump is mechanically chopped at a rate that matches the open/close rate of the CMOS's shutter (up to 1250 Hz). Subsequent probe light is applied to the sample with a delay controlled by an external function generator. Photothermal contrast is then observed by recording differences between "hot" (i.e. pump applied) and "cold" (i.e. no pump applied) frames in acquired CMOS movies.

Figure 6 shows proof-of-concept widefield IR-PHI images. In **Figure 6a** a white light reflection image first reveals the letters MIP written into a PMMA thin film through selective etching of the polymer, which exposes the underlying Si substrate. Next, **Figure 6b** shows the corresponding widefield IR-PHI image observed by exciting PMMA's 1728 cm^{-1} C=O stretching absorption. No signal is seen over etched regions of the film. The attained spatial resolution is 510 nm, as illustrated by the averaged line profile in **Figure 6c**. **Figures 6d-f** show widefield images of d=1 µm PMMA beads deposited onto Si. **Figure 6d** is a reflected light image of three individual beads. **Figure 6e** is the corresponding widefield IR-PHI image acquired using PMMA's 1728 cm^{-1} C=O stretching transition. In **Figure 6e**, an apparent signal-to-noise ratio of ~10 is seen. **Figure 6f** demonstrates IR-PHI's inherent chemical specificity by detuning the pump frequency off the IR resonance of the beads.

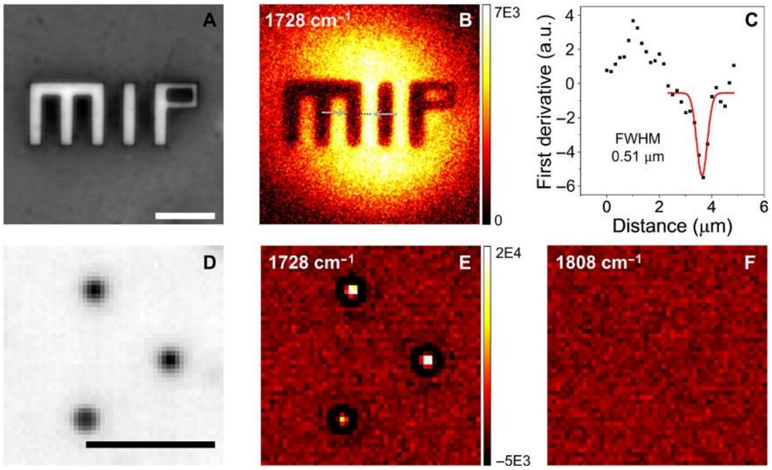

Figure 6. (a) White light reflection image of letters etched into PMMA. (b) Widefield IR-PHI image of the same region acquired by exciting the 1728 cm^{-1} C=O stretching absorption of PMMA. (c) Associated linescan showing an achieved spatial resolution of 510 nm. (d) White light reflection image of three individual *d*=1 μm PMMA beads. (e) Widefield IR-PHI image acquired by exciting the 1728 cm^{-1} C=O stretching absorption of PMMA. (f) Widefield IR-PHI image of the same region acquired off-resonance at 1808 cm^{-1}. Reprinted from https://doi.org/10.1126/sciadv.aav7127. © The Authors, some rights reserved; exclusive licensee American Association for the Advancement of Science. Distributed under a Creative Commons Attribution NonCommercial License 4.0 (CC BY-NC) http://creativecommons.org/licenses/by-nc/4.0/

Other contrast modalities for soft mater systems: Absorption of IR radiation by specimens can be probed optically using other contrast mechanisms beyond photothermal changes to *n* or scattering cross sections. Shi *et al*.[78] have recently used an ultraviolet (UV) photoacoustic detection technique to image IR transitions in lipids and proteins of living cells and mouse brain slices. In their study, an IR pump pulse excites the sample, with two (one before and one after the IR pulse) UV probe pulses used to detect IR pump-induced changes in photoacoustic pressure. Similar to IR-PHI, pump absorption induces a small temperature change in and around the specimen. This changes the magnitude of photoacoustic signals created by the UV pulses. Comparing the photoacoustic signals generated before and after the IR pump pulse therefore provides information about the amount IR light absorbed by the sample. One advantage of photoacoustic detection over other imaging modalities is that water has a small photoacoustic signal so that IR images are readily obtained from biological specimens. Like IR-PHI, the spatial resolution of images is dictated by the probe beam diffraction limit. Consequently, sub-IR diffraction limit spatial resolution is possible.

Another way to detect photothermal changes is to record the phase shifts of light passing through a transparent specimen. Translation of these phase changes into image brighness variations will yield relative photothermal contrast. This information can, in turn, be used to chemically characterize specimens in crowded chemical environments, such as biological samples.[79,80]

IR-PHI imaging and spectroscopy of semiconductors and metals: Beyond above-highlighted advances with soft materials, IR-PHI has been successfully demonstrated on both semiconductors and metals. This is notable because complementary scanning probe techniques such as AFM-IR require thermal expansion of specimens in order to a detect signal. While biological and other soft-matter systems possess fairly large thermal expansion coefficients (e.g. water: α=2.1×10^{-4} m/K[81]), corresponding solid state semiconductors and metals have significantly smaller thermal expansion coefficients (gold: α=1.4×10^{-5} m/K[82], silicon: α=2.6×10^{-6} m/K[83]). This poses a problem for AFM-IR and points to an intrinsic advantage of all-optical approaches such as IR-PHI given their sensitivity to local refractive index differences. For d=5 nm Au nanoparticles in glycerol, Orrit has shown photothermal sensitivity down to Δn~10^{-7}.[48]

The first application of IR-PHI to semiconductors was work by Chatterjee *et al*. to image local cation heterogeneities in mixed cation, hybrid perovskite thin films.[60] This study examined the local composition of $FA_xMA_{1-x}PbI_3$ [formamidinium, FA^+=$CH(NH_2)_2^+$; methylammonium, MA^+=$CH_3NH_3^+$] thin films used to make hybrid perovskite solar cells. Of interest was establishing whether local stoichiometric variations existed in these films given their solution processing. Also of interest was establishing links between any observed compositional differences and local optoelectronic response. **Figures 7a** and **7b** shows results of these measurements, which point to local variations in MA^+ (FA^+) cation stoichiometries within 10×10 μm^2 regions of as made $FA_xMA_{1-x}PbI_3$ films. MA^+ maps were generated using the cation's 1465 cm^{-1} symmetric NH^{3+} bend. FA^+ maps were generated using its 1710 cm^{-1} C=N stretching absorption. **Figure 7c** better highlights observed compositional heterogeneities through a MA^+/FA^+ ratio map. Two dashed circles indicate MA^+ rich (1) and FA^+ rich (2) regions of the film with associated IR-PHI spectra shown in **Figure 7d** (spectra normalized at 1465 cm^{-1}).

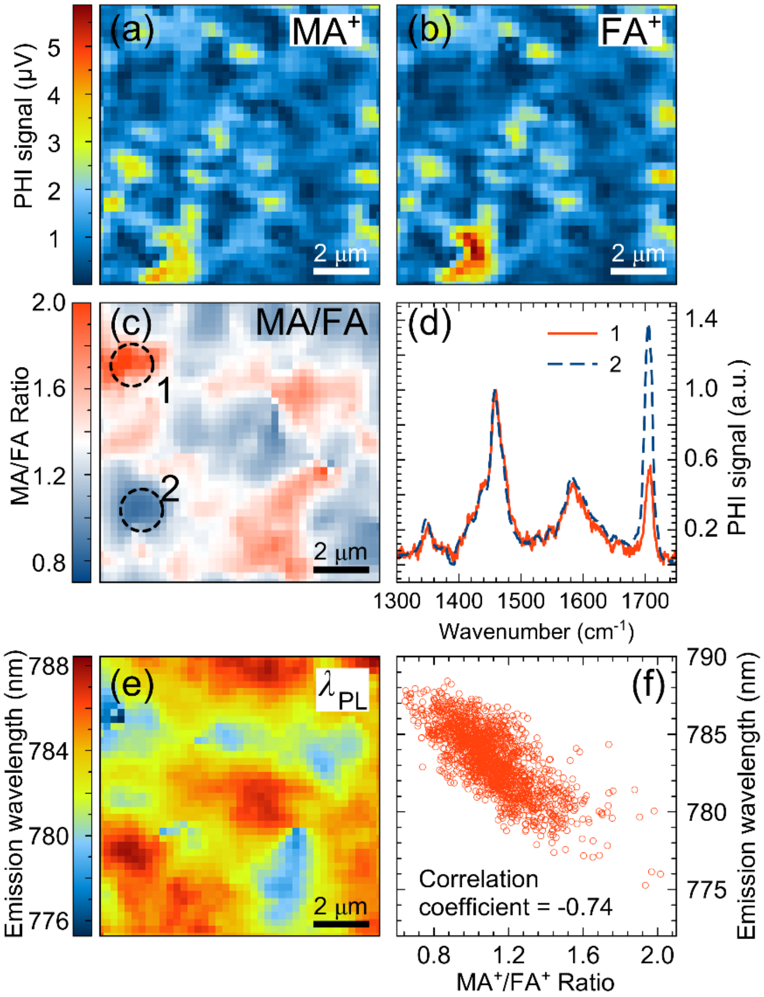

Figure 7. False-color (a) MA^+- and (b) FA^+-specific IR-PHI maps, recorded using the 1465 cm^{-1} (1710 cm^{-1}) transition of MA^+ (FA^+). (c) Corresponding false-color MA^+/FA^+ ratio map. (d) Local IR-PHI spectra obtained at circled points

in (c). (e) Corresponding same area, false-color emission map (λ_{PL}). (f) Pixel correlation plot between (c) and (e), indicating strong correlation between IR-PHI-deduced local composition and band gap.

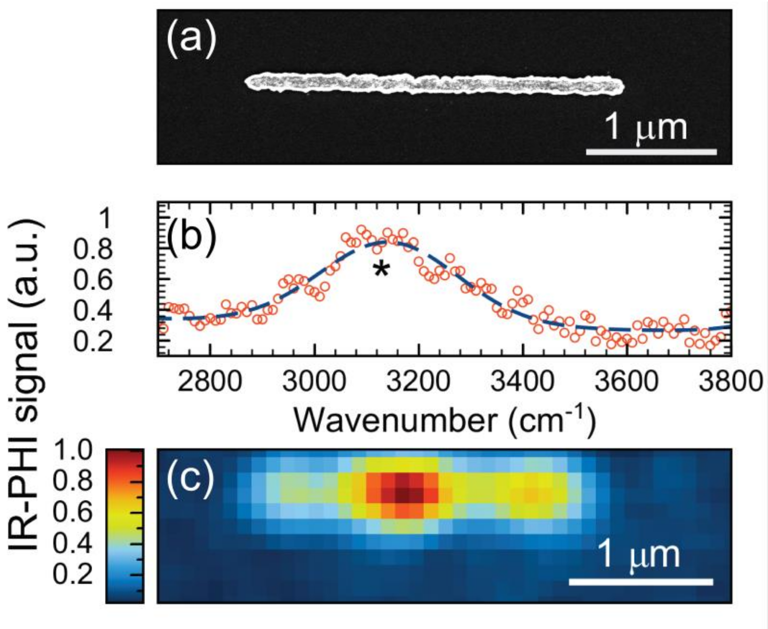

Figure 8. (a) SEM micrograph of a L = 2.9 μm Au NW. (b) Corresponding IR-PHI spectrum, showing a Fabry-Perot plasmon resonance at 3140 cm^{-1} (denoted with an asterisk). (c) IR-PHI image of the same NW.

Importantly, stoichiometric differences translate into $FA_xMA_{1-x}PbI_3$ electronic structure variations. This is shown in **Figure 7e**, which plots local emission wavelength maxima, obtained by fitting acquired emission spectra at each point. The image reveals clear band gap differences across the film with variations of order 25 meV. Visual comparison of **Figures 7c** and **7e** suggest that MA-rich regions of the film have larger band gaps than associated FA-rich regions. This is in line with what is expected as $FAPbI_3$ possesses a smaller band gap than $MAPbI_3$.[84] The link is made stronger through a pixel correlation plot in **Figure 7f**, which reveals a strong inverse correlation between band gap and MA^+/FA^+ ratio. **Figure 7f** thus confirms that local variations in compositional stoichiometry impact hybrid perovskite optical response and ultimately their solar cell performance.

Recently the authors have used IR-PHI to image the mid-IR plasmon resonances of individual, high aspect ratio Au nanowires (NWs).[85] These NWs have been made using nanolithography and possess nominal lengths, L, between L=1-4 μm. Associated widths and heights are $w\approx100$ nm and $h\approx50$ nm. **Figure 8a** is a scanning electron microscope (SEM) image of a representative $L\sim2.9$ μm Au NW. **Figure 8b** shows the NW's corresponding IR-PHI spectrum. Of note is an apparent Fabry-Perot plasmon resonance at 3140 cm^{-1}. In general, NW plasmon resonances are length-dependent and move to lower energies with increasing L. Observed linewidths are also narrow, suggesting suppressed radiation damping and electron-surface scattering in these NWs. The linewidth extracted from **Figure 8b** is 312 cm^{-1}. Finally, **Figure 8c** shows a corresponding IR-PHI image of the wire, revealing that IR-PHI is able to partially resolve the NW's plasmon mode structure. Based on the mode structure in the image, the resonance in Figure 8b is assigned to the m=3 Fabry-Perot mode of the nanowire. Rapid heat diffusion, however, appears to wash out image structure, pointing to areas where IR-PHI can be improved.

IR-PHI limit of detection

We have seen that IR-PHI has the demonstrated ability to conduct high spatial resolution mid-IR imaging and spectroscopy. It is suitable for specimens ranging from soft materials (including those in aqueous environments) to semiconductors and metals. Modifications to IR-PHI have further enabled dynamic imaging of materials. Given this, we now estimate IR-PHI's current limit of detection (LOD).

Figure 9a first shows an IR-PHI image of two *d*=100 nm polystyrene beads, generated by monitoring their 3030 cm^{-1} asymmetric CH_2 stretching absorption. A 532 nm probe and NA=0.95 objective have been used to acquire images in a counter propagating pump/probe geometry with the following experimental conditions: lock-in time constant 30 ms, pixel dwell time 100 ms, pump intensity at the sample 70 kW cm^{-2}, probe intensity 7 MW cm^{-2}. The beads in **Figure 9a** are separated by slightly more than 500 nm and are clearly resolved. This is highlighted in **Figure 9b**, which shows a line profile through the beads (indicated in **Figure 9a**). From Gaussian fits to the linescan, the achieved spatial resolution is ~300 nm. **Figure 9c** highlights the spectral fidelity of IR-PHI by comparing the spectrum of a single *d*=100 nm bead to polystyrene's bulk FTIR spectrum. IR-PHI spectra have been acquired using a 300 ms lock-in time constant, a 1 second dwell time per 2 cm^{-1} wavenumber step, and a total acquisition time of 11 minutes. For comparison, the bulk FTIR spectrum was recorded over the course of 2 minutes.

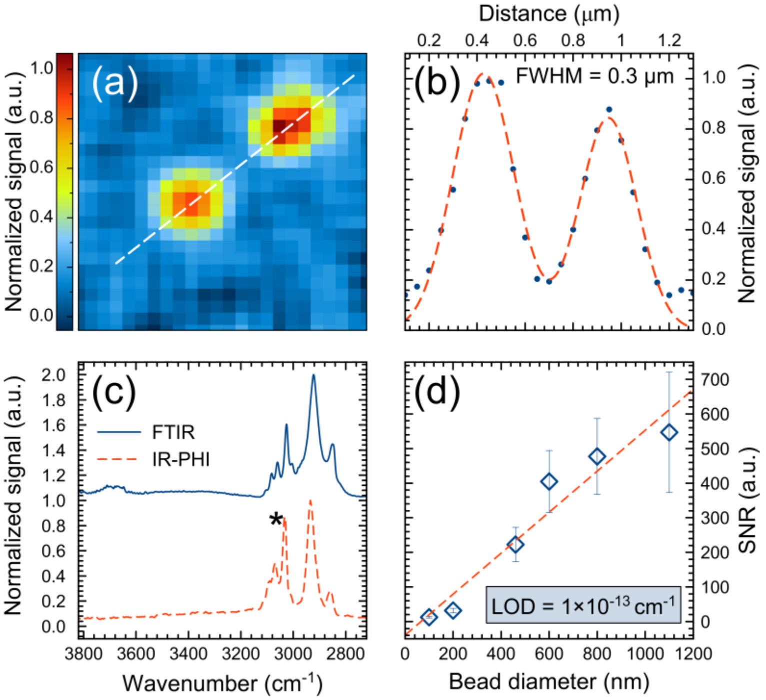

Figure 9. (a) IR-PHI image of individual *d*=100 nm polystyrene beads imaged using their asymmetric CH_2 3030 cm^{-1} stretching mode. (b) Linescan through the beads as indicated by the dashed white line in (a). The dashed red line represents Gaussian fitting of the data. (c) Comparison of the IR-PHI absorption spectrum of a single *d*=100 nm polystyrene bead with its corresponding bulk FTIR spectrum. (d) SNR measured as a function of particle size and linear fit through the data (dashed red line).

In **Figures 9a** and **9b**, an imaging signal-to-noise ratio (SNR) is ~30. This is comparable to the SNR value of ~70 seen in **Figures 4a** and **4b**. Of note though is that much lower pump (probe) intensities were used to acquire the IR-PHI image in **Figure 9a** [70 kW cm^{-2} (7 MW cm^{-2}) versus 840 kW cm^{-2} (18 MW cm^{-2})]. Lock-in time constants were similar (30 ms here versus 10 ms previously). In **Figure 9c**, a SNR of 180 (200) is observed when using polystyrene's asymmetric (symmetric) CH_2 3030 (2930) cm^{-1} transition. This dramatic enhancement of SNR values in spectroscopic measurements arises from using longer lock-in integration times (300 ms to 1 second) to acquire spectra. In all cases, a corresponding *d*=100 nm polystyrene bead 3030 cm^{-1} peak infrared absorption cross section is $\sigma_{3030\ \mathrm{cm}^{-1}} = 4.2 \times 10^{-13}$ cm^2. The above data highlight the sensitivity of IR-PHI's LOD to integration time, pump and probe intensities as well as specimen absorption cross section. These sensitivities have been summarized for visible PHI in Reference 69.

To estimate IR-PHI's current imaging LOD (LOD_{image}), analogous measurements, carried out with the same experimental conditions, have been conducted on *d*=100-1100 nm polystyrene beads. We focus on LOD_{image} since this is the most immediate metric needed by those conducting IR-PHI measurements. Mie theory is used to ~~extract~~ estimate corresponding peak infrared absorption cross sections at 3030 cm^{-1}. **Figure 9d** summarizes results from these measurements by plotting estimated *image* SNR values versus *d*. By fitting the data with a line and defining a LOD_{image} as when SNR=5, an approximate peak absorption cross section LOD_{image} is $\sigma_{3030\ \mathrm{cm}^{-1}} \sim 10^{-13}$ cm^2 [polystyrene 3030 cm^{-1} asymmetric CH_2 stretch, lock-in time constant of 30 ms, and pump (probe) intensity of 70 kW cm^{-2} (7 MW cm^{-2})]. This corresponds to a *d*=70 nm polystyrene bead.

LOD_{image} can be improved by increasing employed lock-in time constants. This, however, comes at the expense of longer experiments. In practice, we therefore suggest that immediate approaches to improving IR-PHI's LOD_{image} involve using slightly longer integration times in conjunction with detectors having lower noise equivalent powers[48], and common-mode noise rejecting schemes like balanced/auto-balanced detection.[73]

Visual summary and comparison to other mid-IR super-resolution techniques

We now summarize in **Figure 10** the different techniques developed to conduct super-resolution mid-infrared microscopy and spectroscopy. Shown are their expected spatial resolutions as well as the instrumental complexity, which correlates with cost. The graphic clearly indicates that STEM-EELS possesses the highest spatial resolution of all methods. However, this comes at high cost and with limited ability to work with specimens under ambient conditions. AFM-IR has very high spatial resolution and unlike STEM-EELS can be applied to studying biological specimens. However, possible reasons why IR-AFM may not be suitable for all measurements is the need to detect IR absorption indirectly through specimen expansion. Adding to this are the generally limited field of view of AFM techniques.

IR-PHI in its various forms represents a low cost, high spatial resolution technique with the flexibility to examine specimens under ambient conditions and in different chemical environments.[52] It has the added capability to conduct large area, dynamic, chemical imaging measurements.[53,61,63]

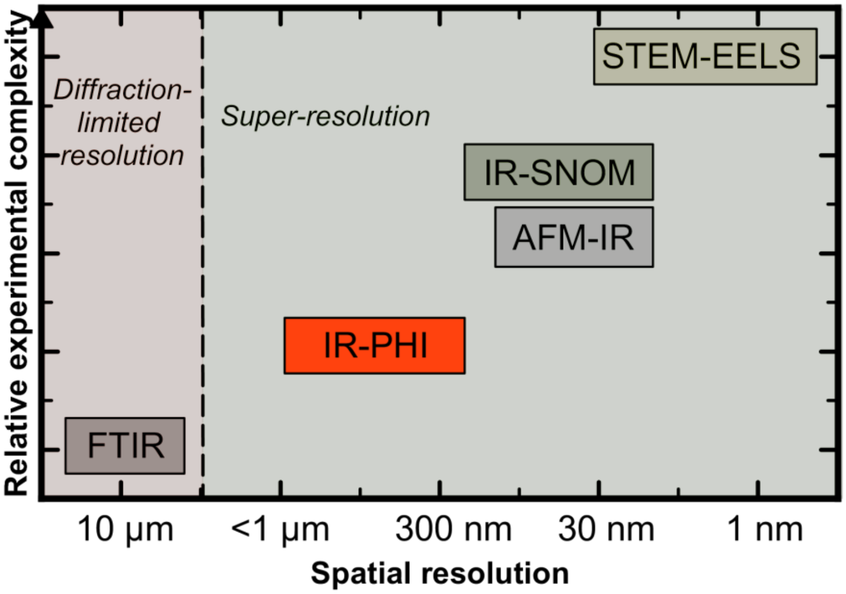

Figure 10. Visual comparison of different mid-IR super-resolution imaging and spectroscopy techniques in terms of their complexity, cost and spatial resolution.

Outlook/Conclusions

The last decade has seen sizable advances in realizing super-resolution imaging and spectroscopy in the all-important, mid-infrared region of the electromagnetic spectrum. IR-PHI is just the latest incarnation of these efforts that now enable researchers to probe materials with chemical specificity and with ever ~~increasing~~ improving limits of detection. Several of the techniques we have discussed have now been commercialized, most notably apertureless IR-SNOM, AFM-IR and IR-PHI. Looking forward, we suggest that the continued refinement of abovementioned techniques portend notable advances in biology, materials science, and plasmonics. We envision that a possible outcome of these efforts will be the eventual realization of vibrational microscopy's ultimate goal: single molecule detection. This would then complement more than two centuries of work in using light/matter interactions to identify, understand and manipulate matter.

Acknowledgements

M.K. and G.V.H thank the U.S. National Science Foundation for financial support of this study through grants CHE-1563528 and CHE-1902403, respectively, and from the University of Notre Dame Faculty Research Program. Any opinions, findings, and conclusions or recommendations expressed in this material are those of the authors and do not necessarily reflect the views of the National Science Foundation.

ORCID numbers

Ilia M. Pavlovetc: 0000-0002-2468-6751

Kyle Aleshire: 0000-0002-9740-0160
Masaru Kuno: 0000-0003-4210-8514
Gregory V. Hartland: 0000-0002-8650-6891

References:

---

[1] K. M. Mayer and J. H. Hafner, Chem. Rev., 2011, **111**, 6, 3828-3857

[2] B. Dragnea, J. Preusser, and W. Schade, and S. R. Leone, J. of Appl. Phys., 1999, **86**, 2795

[3] B. Dragnea and S. R. Leone, Int. Rev. in Phys. Chem., 2001, **20**, 1, 59-92

[4] A. D. Smith, M. R. F. Siggel-King, G. M. Holder, A. Cricenti, M. Luce, P. Harrison, D. S. Martin, M. Surman, T. Craig, S. D. Barrett, A. Wolski, D. J. Dunning, N. R. Thompson, Y. Saveliev, D. M. Pritchard, A. Varro, S. Chattopadhyay, and P. Weightman, Appl. Phys. Lett., 2013, **102**, 053701

[5] D. Vobornik, G. Margaritondo, J. S. Sanghera, P. Thielen, I. D. Aggarwal, B. Ivanov, N. H. Tolk, V. Manni, S. Grimaldi, A. Lisi, S. Rieti, D. W. Piston, R. Generosi, M. Luce, P. Perfetti, and A. Cricenti, J Alloy Compd, 2005, **401**, 1-2, 80-85

[6] A. Lahrech, R. Bachelot, P. Gleyzes, and A. C. Boccara, Opt. Lett., 1996, **21**, 17, 1315-1317

[7] L. Novotny, D. W. Pohl, and P. Reglia, Ultramicroscopy, 1995, **57**, 2-3, 180-188

[8] C. J. Bouwkamp, Philips Research Reports 1950, **5**, 401-422

[9] C. A. Michaels, X. Gu, D. B. Chase, and S. J. Stranick, Appl. Spectrosc., 2004, **58**, 257

[10] J. S. Sanghera, I. D. Aggarwal, A. Cricenti, R. Generosi, M. Luce, P. Perfetti, G. Margaritondo, N. H. Tolk, and D. Piston, IEEE J. Sel. Top. Quantum Electron., 2008, **14**, 5, 1343-1352

[11] R. Hillenbrand, T. Taubner, and F. Keilmann, Nature, 2002, **418**, 159-162

[12] F. Keilmann and R. Hillenbrand, Philos. Trans. Royal Soc. A, 2004, **362**, 1817, 787-805

[13] M. Brehm, A. Schliesser, and F. Keilmann, Opt. Express, 2006, **14**, 23, 11222-11233

[14] J. Chen, M. Badioli, P. Alonso-González, S. Thongrattanasiri, F. Huth, J. Osmond, M. Spasenović, A. Centeno, A. Pesquera, P. Godignon, A. Z. Elorza, N. Camara, F. J. G. de Abajo, R. Hillenbrand, and F. H. L. Koppens, Nature, 2012, **487**, 77-81

[15] A. Cricenti, G. Longo, V. Mussi, R. Generosi, M. Luce, P. Perfetti, D. Vobornik, G. Margaritondo, P. Thielen, J. S. Sanghera, I. D. Aggarwal, N. H. Tolk, G. Baldacchini, F. Bonfigli, F. Flora, T. Marolo, R. M. Montereali, A. Faenov, T. Pikuz, F. Somma, and D. W. Piston, Phys. Stat. Sol. (c), 2003, **0**, 8, 3075–3080

[16] D. E. Halliwell, C. L. M. Morais, K. M. G. Lima, J. Trevisan, M. R. F. Siggel-King, T. Craig, J. Ingham, D. S. Martin, K. A. Heys, M. Kyrgiou, A. Mitra, E. Paraskevaidis, G. Theophilou, P. L. Martin-Hirsch, A. Cricenti, M. Luce, P. Weightman, and F. L. Martin, Sci. Rep., 2016, **6**, 29494

[17] I. M. Craig, M. S. Taubman, A. S. Lea, M. C. Phillips, E. E. Josberger, and M. B. Raschke, Opt. Express, 2013, **21**, 25, 30401-30414

[18] F. Huth, A. Govyadinov, S. Amarie, W. Nuansing, F. Keilmann, and R. Hillenbrand, Nano Lett., 2012, **12**, 8, 3973-3978

[19] S. Bensmann, F. Gaußmann, M. Lewin, J. Wüppen, S. Nyga, C. Janzen, B. Jungbluth, and T. Taubner, Opt. Express, 2014, **22**, 19, 22369-22381

[20] B. T. O'Callahan, W. E. Lewis, S. Möbius, J. C. Stanley, E. A. Muller, and M. B. Raschke, Opt. Express, 2015, **23**, 25, 32063-32074

[21] M. Wagner, D. S. Jakob, S. Horne, H. Mittel. S. Osechinskiy. C. Phillips, G. C. Walker, C. Su, and X. G. Xu, ACS Photonics, 2018, **5**, 4, 1467-1475

[22] I. Amenabar, S. Poly, W. Nuansing, E. H. Hubrich, A. A. Govyadinov, F. Huth, R. Krutokhvostov, L. Zhang, M. Knez, J. Heberle, A. M. Bittner, and R. Hillenbrand, Nat. Comm., 2013, **4**, 2890

[23] M. Schnell, A. García-Etxarri, A. J. Huber, K. Crozier, J. Aizpurua, and R. Hillenbrand, Nat. Phot., 2009, **3**, 287–291

[24] F. Zenhausern, Y. Martin, H. K. Wickramasinghe, Science, 1995, **269**, 5227, 1083-1085

[25] J.-J. Greffet and R. Carminati, Prog. Surf. Sci., 1997, 56, 3, 133-237

[26] R. C. Dunn, Chem. Rev.1999, **99**, 10, 2891-2928

[27] H. A. Bechtel, E. A. Muller, R. L. Olmon, M. C. Martin, and M. B. Raschke, Proc. Natl. Acad. Sci. U.S.A., 2014, **111**, 20, 7191-7196

[28] R. W. Johns, H. A. Bechtel, E. L. Runnerstrom, A. Agrawal, S. D. Lounis, and D. J. Milliron, Nature Comm., 2016, **7**, 11583

[29] D. Rossouw and G. A. Botton, Phys. Rev. Lett., 2013, **110**, 066801

[30] J. A. Hachtel, A. R. Lupini, and J. C. Idrobo, Sci. Rep., 2018, **8**, 5637

[31] J. Park, S. Heo. J.-G. Chung, H. Kim, H. Lee, K. Kim, and G.-S. Park, Ultramicroscopy, 2009, **109**, 9, 1183-1188

[32] J. A. Scholl, A. L. Koh, and J. A. Dionne, Nature, 2012, **483**, 421-427

---

[33] G. Li, C. Cherqui, N. W. Bigelow, G. Duscher, P. J. Straney, J. E. Millstone, D. J. Masiello, and J. P. Camden, Nano Lett., 2015, **15**, 5, 3465-3471

[34] O. L. Krivanek, T. C. Lovejoy, N. Dellby, T. Aoki, R. W. Carpenter, P. Rez, E. Soignard, J. Zhu, P. E. Batson, M. J. Lagos, R. F. Egerton, and P. A. Crozier, Nature, 2014, **514**, 209-212

[35] N. Mirsaleh-Kohan, V. Iberi, P. D. Simmons, Jr., N. W. Bigelow, A. Vaschillo, M. M. Rowland, M. D. Best, S. J. Pennycook, D. J. Masiello, B. S. Guiton, and J. P. Camden, J. Phys. Chem. Lett., 2012, **3**, 16, 2303-2309

[36] A. A. Govyadinov, A. Konečná, A. Chuvilin, S. Vélez, I. Dolado, A. Y. Nikitin, S. Lopatin, F. Casanova, L. E. Hueso, J. Aizpurua, and R. Hillenbrand, Nature Comm., 2017, **8**, 95

[37] M. Bosman, E. Ye, S. F. Tan, C. A. Nijhuis, J. K. W. Yang, R. Marty, A. Mlayah, A. Arbouet, C. Girard, and M.-Y. Han, Sci. Rep., 2013, **3**, 1312

[38] M. J. Lagos, A. Trügler, U. Hohenester, and P. E. Batson, Nature, 2017, **543**, 529-532

[39] A. M. Katzenmeyer, G, Holland, K. Kjoller, and A. Centrone, Anal. Chem. 2015, **87**, 6, 3154-3159

[40] A. Dazzi and C. B. Prater, Chem. Rev. 2017, **117**, 7, 5146-5173

[41] L. Wang, H. Wang, M. Wagner, Y. Yan, D. S. Jakob, and X. G. Xu, Sci. Adv., 2017, **3**, 6, e1700255

[42] F. Lu, M. Jin, and M. A. Belkin, Nature Phot., 2014, **8**, 307-312

[43] S. Karrasch, R. Hegerl, J. H. Hoh, W. Baumeister, and A. Engel, Proc. Natl. Acad. Sci. U.S.A., 1994, **91**, 3, 836-838

[44] J. R. Felts, S. Law, C. M. Roberts, V. Podolskiy, D. M. Wasserman, and W. P. King, Appl. Phys. Lett., 2013, **102**, 152110

[45] J. Houel, S. Sauvage, P. Boucaud, A. Dazzi, R. Prazeres, F. Glotin, J.-M. Ortéga, A. Miard, and A. Lemaître, Phys. Rev. Lett., 2007, **99**, 217404

[46] J. J. Schwartz, H.-J. Chuang, M. R. Rosenberger, S. V. Sivaram, K. M. McCreary, B. T. Jonker, and A. Centrone, ACS Appl. Mater. Interfaces, 2019, **11**, 28, 25578-25585

[47] S. Clède, F. Lambert, C. Sandt, S. Kascakova, M. Unger, E. Harté, M.-A. Plamont, R. Saint-Fort, A. Deniset-Besseau, Z. Gueroui, C. Hirschmugl, S. Lecomte, A. Dazzi, A. Vessières, and C. Policar, Analyst, 2013, **138**, 5627-5638

[48] A. Gaiduk, P. V. Ruijgrok, M. Yorulmaz, and M. Orrit, Chem. Sci., 2010, **1**, 343-350

[49] J. M. Jewell, C. Askins, and I. D. Aggarwal, Appl. Opt., 1991, **30**, 25, 3656-3660

[50] C. Li, D. Zhang, M. N. Slipchenko, and J.-X. Cheng, Anal. Chem., 2017, **89**, 9, 4863-4867

[51] E. S. Lee and J. Y. Lee, Appl. Phys. Lett., 2009, **94**, 261101

[52] D. Zhang, C. Li, C. Zhang, M. N. Slipchenko, G. Eakins., and J.-X. Cheng, Sci. Adv., 2016, **2**, 9, e1600521

[53] Z. Li, K. Aleshire, M. Kuno, G. V. Hartland, J. Phys. Chem. B, 2017, **121**, 37, 8838-8846

[54] D. Boyer, P. Tamarat, A. Maali, B. Lounis, M. Orrit, Science, 2002, **297**, 5584, 1160-1163

[55] S. Berciaud, L. Cognet, G. A. Blab, and B. Lounis, Phys. Rev. Lett., 2004, **93**, 257402

[56] S. Berciaud, D. Lasne, G. A. Blab, L. Cognet, and B. Lounis, Phys. Rev. B, 2006, **73**, 045424

[57] A. Mërtiri, T. Jeys, V. Liberman, M. K. Hong, J. Mertz, H. Altug, and S. Erramilli, Appl. Phys. Lett., 2012, **101**, 044101

[58] A. Totachawattana, H. Liu, A. Mertiri, M. K. Hong, S. Erramilli, and M. Y. Sander, Opt. Lett., 2016, **41**, 1, 179-182

[59] P. D. Samolis and M. Y. Sander, Opt. Expr., 2019, **27**, 3, 2643-2655

[60] R. Chatterjee, I. M. Pavlovetc, K. Aleshire, G. V. Hartland, and M. Kuno, ACS Energy Lett., 2018, **3**, 2, 469-475

[61] Y. Bai, D. Zhang, L. Lan, Y. Huang, K. Maize, A. Shakouri, and J.-X. Cheng, Sci. Adv., 2019, **5**, 7, eaav7127

[62] Y. Bai, D. Zhang, C. Li, C. Liu, and J.-X. Cheng, J. Phys. Chem. B, 2017, **121**, 44, 10249-10255

[63] J. M. Lim, C. Park, J.-S. Park, C. Kim, B. Chon, and M. Cho, J. Phys. Chem. Lett., 2019, **10**, 11, 2857-2861

[64] J. Giblin, M. Syed, M. T. Banning, M. Kuno, and G. Hartland, ACS Nano, 2010, **4**, 1, 358-364

[65] E. S. Lee and J. Y. Lee, Opt. Express, 2011, **19**, 2, 1378-1384

[66] X. Li, D. Zhang, Y. Bai, W. Wang, J. Liang, J.-X. Cheng, Anal. Chem., 2019, **91**, 16, 10750-10756

[67] M. Zahedian, E. S. Koh, and B. Dragnea, Appl. Opt., 2019, 58, 27, 7352-7358

[68] E. Hecht, *Optics*, Pearson, New York, 6th edn, 2016

[69] R. Chatterjee, I. M. Pavlovetc, K. Aleshire, and M. Kuno, J. Phys. Chem. C, 2018, **122**, 29, 16443-16463

[70] M. Selmke, M. Braun, and F. Cichos, ACS Nano, 2012, **6**, 3, 2741-2749

[71] A. Arbouet, D. Christofilos, N. Del Fatti, F. Vallée, J. R. Huntzinger, L. Arnaud, P. Billaud, and M. Broyer, Phys. Rev. Lett., 2004, **93**, 127401

[72] J. Giblin, F. Vietmeyer, M. P. McDonald, and M. Kuno, Nano Lett., 2011, **11**, 8, 3307-3311

[73] M. P. McDonald, F. Vietmeyer, D. Aleksiuk, and M. Kuno, Rev. Sci. Instrum., 2013, **84**, 113104

[74] F. Vietmeyer, R. Chatterjee, M. P. McDonald, and M. Kuno, Phys. Rev. B, 2015, **91**, 085422

---

[75] M. P. McDonald, R. Chatterjee, J. Si, B. Jankó, and M. Kuno, Nature Comm., 2016, **7**, 12726

[76] G. Steinbach, I. Pomozi, O. Zsiros, L. Menczel, and G. Garab, Acta Histochemica, 2009, **111**, 4, 317-326

[77] C. R. Carey, T. LeBel, D. Crisostomo, J. Giblin, M. Kuno, and G. V. Hartland, J. Phys. Chem. C, 2010, **114**, 38, 16029-16036

[78] J. Shi, T. T. W. Wong, Y. He, L. Li, R. Zhang, C. S. Yung, J. Hwang, K. Maslov, and L. V. Wang, Nat. Phot., 2019, **13**, 609-615

[79] K. Toda, M. Tamamitsu, Y. Nagashima, R. Horisaki, and T. Ideguchi, Sci. Rep., 2019, **9**, 9957

[80] D. Zhang, L. Lan, Y. Bai, H. Majeed, M. E. Kandel, G. Popescu, and J.-X. Cheng, Light Sci. Appl., 2019, **8**, 116

[81] L. G. Hepler, Can. J. Chem., 1969, **47**, 24, 4613-4617

[82] F. C. Nix and D. MacNair, Phys. Rev., 1941, **60**, 597

[83] Y. Okada and Y. Tokumaru, J. Appl. Phys., 1984, **56**, 314

[84] L. K. Ono, E. J. Juarez-Perez, and Y. Qi, ACS Appl. Mater. Interfaces, 2017, **9**, 36, 30197-30246

[85] K. Aleshire, I. M. Pavlovetc, R. Collette, X.-T. Kong, P. D. Rack, S. Zhang, D. J. Masiello, J. P. Camden, G. V. Hartland, and M. Kuno, https://doi.org/10.1073/pnas.1916433117